The 2015 Gorkha (Nepal) earthquake sequence: I. Source modeling and deterministic 3D ground shaking

8 authors, including:

Shengji Wei
California Institute of Technology
70 PUBLICATIONS **1,662** CITATIONS

SEE PROFILE

Xin Wang
California Institute of Technology
12 PUBLICATIONS **82** CITATIONS

SEE PROFILE

Eric O. Lindsey
Nanyang Technological University
26 PUBLICATIONS **461** CITATIONS

SEE PROFILE

Teng Wang
Nanyang Technological University
62 PUBLICATIONS **962** CITATIONS

SEE PROFILE

Some of the authors of this publication are also working on these related projects:

Project Study of Broadband Records from the TERRAscope Array, California View project

Project Fault geometry inferred by broadband waveform modeling View project

The 2015 Gorkha (Nepal) earthquake sequence: I. Source modeling and deterministic 3D ground shaking

Shengji Wei[a,b,*], Meng Chen[a,b], Xin Wang[a,b], Robert Graves[c], Eric Lindsey[a,b], Teng Wang[a,b], Çağıl Karakaş[a,b], Don Helmberger[d]

[a] Earth Observatory of Singapore, Nanyang Technological University, Singapore
[b] Asian School of the Environment, Nanyang Technological University, Singapore
[c] U. S. Geological Survey, Pasadena, CA, USA
[d] Seismological Laboratory, California Institute of Technology, CA, USA

A B S T R A C T

To better quantify the relatively long period (< 0.3 Hz) shaking experienced during the 2015 Gorkha (Nepal) earthquake sequence, we study the finite rupture processes and the associated 3D ground motion of the Mw7.8 mainshock and the Mw7.2 aftershock. The 3D synthetics are then used in the broadband ground shaking in Kathmandu with a hybrid approach, summarized in a companion paper (Chen and Wei, 2017, submitted together). We determined the coseismic rupture process of the mainshock by joint inversion of InSAR/SAR, GPS (static and high-rate), strong motion and teleseismic waveforms. Our inversion for the mainshock indicates unilateral rupture towards the ESE, with an average rupture speed of 3.0 km/s and a total duration of ~60 s. Additionally, we find that the beginning part of the rupture (5–18 s) has about 40% longer rise time than the rest of the rupture, as well as slower rupture velocity. Our model shows two strong asperities occurring ~24 s and ~36 s after the origin and located ~30 km to the northwest and northeast of the Kathmandu valley, respectively. In contrast, the Mw7.2 aftershock is more compact both in time and space, as revealed by joint inversion of teleseismic body waves and InSAR data. The different rupture features between the mainshock and the aftershock could be related to difference in fault zone structure. The mainshock and aftershock ground motions in the Kathmandu valley, recorded by both strong motion and high-rate GPS stations, exhibited strong amplification around 0.2 Hz. A simplified 3D basin model, calibrated by an Mw5.2 aftershock, can match the observed waveforms reasonably well at 0.3 Hz and lower frequency. The 3D simulations indicate that the basin structure trapped the wavefield and produced an extensive ground vibration. Our study suggests that the combination of rupture characteristics and propagational complexity are required to understand the ground shaking produced by hazardous earthquakes such as the Gorkha event.

1. Introduction

The Mw7.8 Gorkha earthquake (25 April 2015) and its Mw7.2 aftershock (12 May 2015) are the largest events to have occurred on the Main Himalayan Thrust (MHT) since the great 1934 Mw8.2 Bihar-Nepal earthquake (Fig. 1) (Sapkota et al., 2013). This earthquake sequence unzipped the lower edge of the locked portion of the MHT (Avouac et al., 2015), along which India underthrusts the Himalayas and Southern Tibet at a rate of ~18 mm/yr (Lave and Avouac, 2000). Geologic investigations combined with geophysical experiments reveal a complex plate interface geometry where deformation is accommodated along a laterally varying sequence of ramps whose relation with a series of destructive earthquakes is poorly understood (Bettinelli et al., 2006; Bollinger et al., 2004; Cattin and Avouac, 2000).

The 1934 Mw8.2 earthquake ruptured a relatively flat portion of the MHT just east of the Kathmandu Valley (Sapkota et al., 2013) and produced severe damage and many casualties in Kathmandu (Sapkota et al., 2016). The 2015 earthquake occurred at the western edge of the 1934 rupture area, immediately beneath the Kathmandu Valley (Fig. 1). While nearly 9000 lives were lost throughout Nepal during the 2015 earthquake, surprisingly little damage and loss of life occurred in Kathmandu, especially in light of the previous experience in 1934. The relatively low damage levels in Kathmandu suggest that the ground motions were weaker than expected for an Mw7.8 earthquake at this distance (Galetzka et al., 2015), although the estimated intensities show some variations (Martin et al., 2015; McGowan et al., 2017). In order to
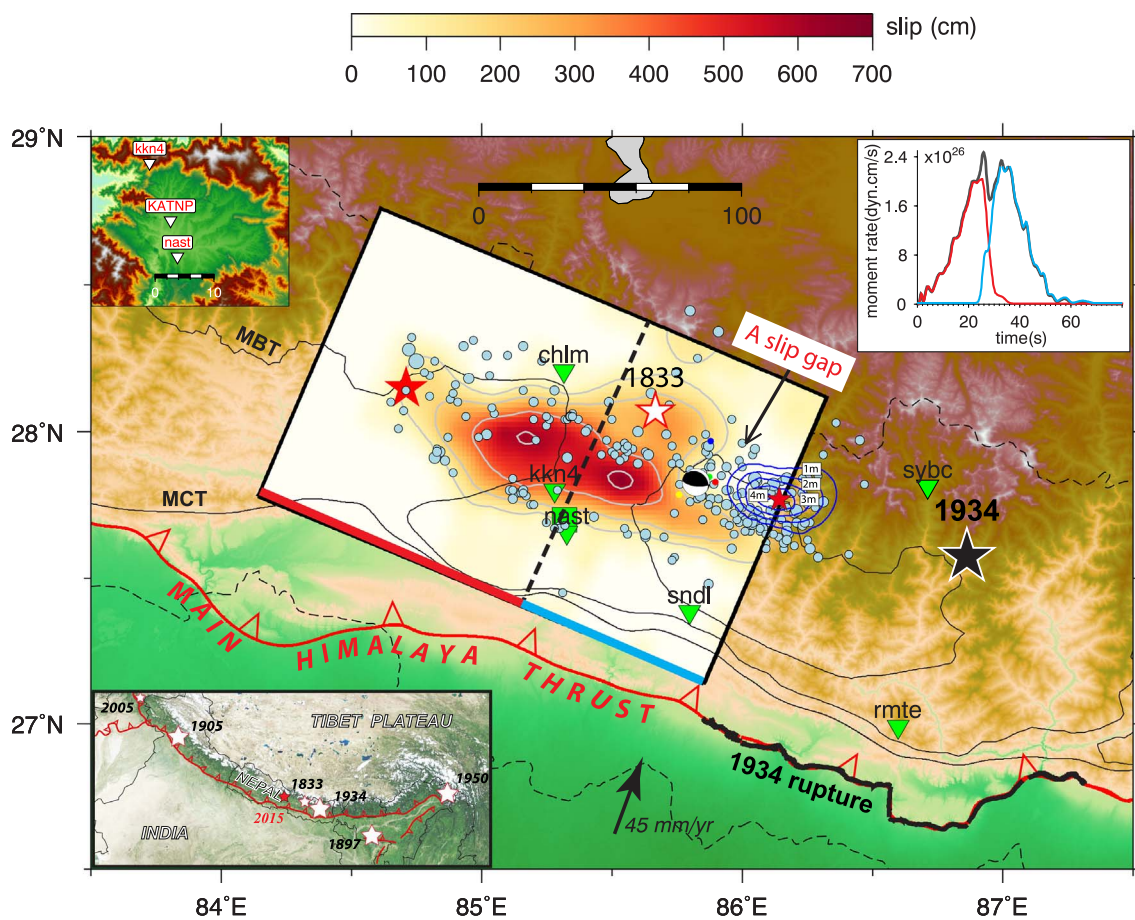
Fig. 1. Overview of the 2015 Nepal earthquake sequence. The GPS and strong motion stations are shown as green triangles with zoom-in of Kathmandu region shown in the upper left. The circles are the seismicity in the first three months. The slip model of the 2015 M7.8 mainshock is color-coded and the blue contours indicate the slip model of the Mw7.2 aftershock. The Main Himalayan Thrust is shown as the red line, with other thrust faults indicated as MBT = Main Boundary Thrust and MCT = Main Central Thrust. The epicenters of the 1833 Mw7.8 and the 1934 Mw8.2 earthquakes are plotted as white and black stars respectively, and the epicenter of the 2015 event is shown by the red star. Surface rupture of the 1934 event is shown as black heavy lines. The focal mechanism beach ball indicates the location of the Mw5.2 aftershock, which was used to established path calibration. The moment-rate function is shown in the upper-right inset with red and blue lines indicate the contribution from the first and the second asperities that are separated by the dash line the map view. A regional map with large seismic events is plotted in the lower-left.

explain these observations, we need a better understanding of the rupture properties of the 2015 earthquake sequence as well as the geologic structure beneath Kathmandu. In this paper, we focus on deriving the kinematic rupture models for the mainshock and the Mw7.2 aftershock. The 3D deterministic synthetics obtained in this study are combined with stochastic synthetics through a hybrid approach to simulate the broadband ground shaking in Kathmandu both for the mainshock and the Mw7.2 aftershock, which are summarized in a companion paper (Chen and Wei, 2017, submitted together).

So far, a number of papers have been published on the source properties of the earthquake using seismological and geodetic data, either individually or jointly. Among these studies, Wang and Fialko (2015), Elliott et al. (2016) and Feng et al. (2015) used ALOS2 InSAR images and static GPS data to study the slip distribution of the mainshock and the Mw7.2 aftershock; and (Avouac et al., 2015), Grandin et al. (2015), Galetzka et al. (2015), Yagi and Okuwaki (2015), Liu et al. (2016), Lay et al. (2017), Yue et al. (2017) and Hayes et al. (2015), derived kinematic rupture models of the mainshock using high-rate GPS waveform, strong motion data and/or teleseismic body waves. Most of these kinematic inversions also include geodetic data (e.g. ALOS2 InSAR data), which provide additional constraints on the spatial distribution of the static slip because of the high quality and comprehensive spatial coverage of the data. To constrain the temporal evolution of the rupture (i.e. rupture speed and rise time), all these studies used either high-rate GPS, strong motion data at local distance or P and SH

waves at teleseismic distance, but none use all data sets except Grandin et al. (2015). Additionally, the waveform inversion in Liu et al. (2016) and Grandin et al. (2015) were conducted at relatively long period, i.e. 10s and longer period for local waveform data and 8 s and longer period for teleseismic body waves, and use displacement data in the inversion process.

Galetzka et al. (2015) inverted for the rise time of the mainshock using local high-rate GPS and strong motion data and concluded that the average rise time is around 6 s with the time to the peak slip rate of 1.7 s, suggesting an asymmetric slip-rate function characterized by a fast onset followed by a relatively long tail. But because the strong motion and high-rate GPS stations are very sparsely distributed in the source region, the resolution of the temporal evolution of the earthquake is mainly controlled by the portion of the rupture closest to the stations. To extend these analyses, we resolve the rupture process of the earthquake by jointly inverting local and teleseismic waveform data to higher frequency than the above efforts. We also include the geodetic data (static GPS, SAR and InSAR offsets) in our inversion, which provides a strong constraint on the static slip distribution and thus can minimize the trade-offs between static slip and other source parameters.

As pointed out by some previous studies (Ji et al., 2002; Wei et al., 2013), there can be a strong trade-off between rupture speed and rise time when inverting for rupture properties. Nonetheless, the back-projection of teleseismic high-frequency P-waves indicates that rupture

Table 1
1-D velocity model in the source region.

Thickness (km)	Vs (km/s)	Vp (km/s)	Density (g/cm^3)
4.00	3.20	5.50	2.53
12.00	3.40	5.85	2.64
4.00	3.50	6.00	2.69
6.50	3.70	6.45	2.83
10.00	3.85	6.65	2.90
5.00	4.15	7.20	3.07
14.00	4.20	7.50	3.17
–	4.30	7.90	3.30

speed of the mainshock ranges from 2.8–3.3 km/s (Avouac et al., 2015; Fan and Shearer, 2015; Grandin et al., 2015; Lay et al., 2017; Yagi and Okuwaki, 2015). The consistency between different studies and the narrow range of the rupture speed suggest a smooth rupture process. The back-projection constraints on the rupture speed, together with the geodetic data, provide a unique opportunity for us to resolve the spatial and temporal rupture features in greater detail than is usually possible for most megathrust earthquakes.

Using our refined source model of the mainshock, as well as after-shock data, we also address the ground shaking in and around Kathmandu Valley with the goal of better understanding which features are related to source and path effects. Galetzka et al. (2015) has shown that the ground shaking within the Valley has a dominant frequency around 0.2 Hz (5 s), presumably due to the basin structure producing strong amplification and resonance at this frequency. The ground shaking of some aftershocks, e.g. the Mw7.2 aftershock, also shows similar features, with an even longer duration of strong shaking. Currently, a detailed 3D velocity model of the Kathmandu Valley region is not available, although Paudyal et al. (2013) has reported the thickness of soft sediment in the Kathmandu Basin using microtremor observations. Using these data, we construct a simple model of the 3D basin structure in order to test the impact of the rupture and localized basin response on the (< 0.3 Hz) ground motion within the Kathmandu basin.

In the sections that follow, we will first show the finite fault inversion of the mainshock and the Mw7.2 aftershock, with emphasis on the joint usage of geodetic and seismic data to resolve the rupture details. We then use the derived rupture models along with a simplified 3D velocity model for the Kathmandu Valley to simulate the low frequency (< 0.3 Hz) ground shaking with a 3D finite-difference algorithm.

2. Datasets and processing

To conduct the joint inversion for the finite fault of the mainshock, we collect waveform data at both local distances, including the strong motion waveform data and high-rate GPS data, and teleseismic distances (P and SH body waves), as well as the static GPS offsets, InSAR and SAR data.

We downloaded GSN broadband data from the IRIS DMC and selected 40 teleseismic P and 37 SH waveforms to include in our analysis based upon data quality and azimuthal distribution. Waveforms are first converted to velocity by removing the instrument response at the frequency range lower than 1 Hz. We also downloaded the strong motion data from the Center for Engineering Strong Motion Data (www.strongmotioncenter.org). The original data is integrated once to velocity and filtered at 2 s and longer period. The high-rate GPS data (Galetzka et al., 2015) is differentiated once to velocity and also filtered to the same frequency band as the strong motion data.

In the joint inversion, we also used two SAR/InSAR data pairs (ascending path P157 and descending path P48) from Advanced Land Observing Satellite 2 (ALOS-2) and two pairs (descending Path 19 and ascending Path 85) of Sentinel-1A Synthetic Aperture Radar (SAR)

images. The original data were downsampled to 263 and 715 points in azimuth and range from the descending track P19, and 499 and 786 data points from the ascending track P85, in azimuth and range, respectively. For ALOS-2 P157 azimuthal and P48 range offsets, we downsampled to 288 and 1982 data points, respectively. Here we used more data points for P48 because it covers a much larger area of the deformation field and also because the data quality is better than for the other images. These SAR/InSAR data provide key constraints on the slip distribution of the earthquake, as discussed later. More geodetic data processing details can be found in the appendix.

3. Methodology

We approximate the fault geometry with a planar fault segment having a strike of 293° and dip of 7° (GCMT), and a total length and width of 184 km and 120 km, respectively. This fault is discretized into 8×8 km² subfaults. The crustal structure in this region is approximated by a 1D model (Table 1), which has been used in locating local events and tested against more complex structures (Mahesh et al., 2013). This 1D model was used to generate the Green's functions for local and teleseismic distances. The distributed fault model assumes that the rupture consists of a propagating rupture front with slip accruing in the wake of the passage of the rupture front. The slip history at each grid point (j,k) on the fault is represented by the slip-rate function $[\dot{S}_{jk}(t)]$ which specifies how a point on the fault slips in time. This function is parameterized with a certain shape and duration of slip, the so-called rise-time. In our inversions, we consider both a symmetric cosine slip-rate function and an asymmetric Kostrov-shape function. For each subfault, we solve for the slip amplitude, rake, rise time and the averaged rupture velocity (rupture time).

The determination of a finite fault rupture model is an under-determined problem due to the large number of unknowns and numerous trade-offs among model parameters, such as rise time and rupture velocity. In the present case the trade-offs between asperity location and rupture speed can be significantly reduced if coseismic geodetic observations are available and inverted jointly with the seismological data. This is because the geodetic data are primarily sensitive to the location of large slip patches, whereas the seismological data are also sensitive to the temporal aspects of the rupture. Even so, the determination of a finite fault source remains generally underdetermined if the fault discretization is too fine. One way to regularize the inversion is by setting some constraints on the roughness of the slip distribution, which is the approach adopted here. We have tested the subfault sizes of 10 km * 10 km and 8 km * 8 km, and we find that the latter is more suitable as such subfault size shows more details of the rupture while it does not over-fit the data.

We define the best-fit model as having the lowest objective function similar as in (Ji et al., 2002), given as:

$$\text{Misfit} = \text{Ewf} + \text{WI} * \text{EI} + \text{WS} * \text{S} + \text{Ww} * \text{M},$$

where Ewf is the waveform misfit defined in wavelet domain (Ji et al., 2002), EI is the geodetic misfit, S is a normalized, second derivative of slip between adjacent patches (a so-called Laplacian smoothing), M is a normalized seismic moment, and WI, WS and Ww are the relative weights applied to the geodetic misfit, smoothing, and moment, respectively (Ji et al., 2002). The least squares misfits are calculated for the teleseismic and geodetic data. We tested different values of WI, and found that by varying the weight between 2 and 0.5 did not significantly degrade the fits to the teleseismic or geodetic data for either the individual or joint inversions, as shown in the Supplement Fig. S1. Thus we weighted the geodetic and the seismic data equally, which is realized by normalizing the misfit of each data set by the minimum misfit obtained by inverting the individual dataset. Within the waveform data, we weighted each local station five times larger than that for the teleseismic body waveforms. The static Green's Functions at the free surface are calculated by using the same 1D velocity model (Table 1) as

used in the teleseismic body-wave calculation.

We use a simulated annealing algorithm to find the best fitting model parameters for the joint inversions (Ji et al., 2002). This non-linear, iterative inversion algorithm is designed to avoid local minima by searching broadly through parameter space in initial steps, and then in later iterations to focus on regions that fit the data well.

During the inversion we allow the rake to vary from 90° to 130°, and the slip amplitude is capped at 10 m. We selected the range for the rupture speed to be 2.5–3.5 km/s, which agrees with the back-projection results (Avouac et al., 2015; Fan and Shearer, 2015; Yagi and Okuwaki, 2015). We adopt the USGS epicenter location (http://earthquake.usgs.gov/earthquakes/map/) in the inversion, but we place the hypocenter at 12 km instead of 15 km as used in other studies. This is because a shallower fault plane is needed to better fit the InSAR and SAR data, as well as being more consistent with the depth of aftershocks and geologic structure (e.g. Hubbard et al., 2016; Wang et al., 2017) (also discussed further below).

4. Mainshock results

The joint inversion result using the cosine source time function is presented in Figs. 1 and 2. Here, the range of rise times allowed was bracketed by 1 s to 11 s with most values determined to be near 4 s. Our model shows that the earthquake ruptured unilaterally towards the east-southeast (Fig. 2b). The beginning of the rupture (5–18 s) has about 40% longer rise times than the rest of the rupture (Fig. 2a).

After the first 15 s, when the rupture front is ~40 km to the east of the epicenter, the earthquake ruptured the first major asperity, located between high-rate GPS stations CHLM and KKN4 (Figs. 1, 2a,b). This part of the rupture made the major contribution to the strong motion stations close to the asperity (Fig. S1, e.g. KKN4 and CHLM). As the rupture continued, the second major asperity broke, located about 30 km to the east of KKN4. These two major asperities correspond to the two peaks in the moment-rate function (Fig. 1, inset), centered at ~24 s and ~36 s, respectively. These two asperities are corresponding to the two peaks in most of the strong motion/high-rate GPS data (Fig. S2). The distance away from the rupture and the rupture directivity effect controls the varying amplitude ratios of these two peaks. The rupture also propagated about 30 km to the north of the second asperity, as well as towards the east along a narrower strip (~20 km) extending about 40 km from the eastern end of the second major asperity. The northward and eastward rupture form an abrupt corner of slip gap, in which many of the aftershocks took place. The rise times for the rupture after 18 s are quite consistent, which show an average duration of ~6 s for the cosine-shape source time function. The total duration of the earthquake is about 60 s and the along strike rupture dimension is about 140 km. The along dip dimension varies along the strike; the widths of two major asperities are about 30 km each.

The fit to the static GPS offsets, P157 (ALOS-2) azimuthal offsets and P48 (ALOS-2) range offsets are displayed in Fig. 3. More fits to the

Sentinal-1 data can be found in Fig. S3. Similar to previous studies, the agreement between data and synthetics is quite good. Although slip distribution characteristics are quite similar to those found earlier (Fig. 1, map view), they have sharper features and are closer to the surface, due to the constraint from the additional geodetic data. We find that a shallower fault plane with hypocenter depth of 12 km provides a much better fit to the geodetic observations, also in agreement with refined aftershock seismicity and geology profiles (e.g. Hubbard et al., 2016; Wang et al., 2017). This is particularly true for the azimuthal offset data as shown in Fig. 3. For comparison, setting the fault deeper such that the hypocenter is located at 15 km as in the early USGS report does not fit these data as well (Fig. 3c). The USGS hypocenter was refined to 9 km a couple months after the earthquake, which is shallower than our preferred value.

The teleseismic and local velocity waveform fits are shown in Figs. 4 and 5. Overall we have very good fits for the strong motion and high-rate GPS waveforms except the horizontal components of KATNP and nast stations. These stations are located within the Kathmandu basin and we will address this issue in the following sections. Also note the very strong directivity effect as shown in both the teleseismic waveform data and the synthetics. This can be observed in the SH-waveform data by comparing the two boxes in Fig. 4. Since the event is propagating towards the east, we would expect stronger amplitudes and shorter duration motions for sites located to the east of the rupture (lower box), compared to sites located in the opposite direction (upper box). Such features are not observed for the more concentrated Mw7.2 aftershock addressed later. In our inversion, we used velocity records for the teleseismic waveforms instead of displacement in order to emphasize the higher frequency content in the recorded motions. Integrating these waveforms, we find the simulated teleseismic displacements provide an excellent fit to the observed teleseismic displacements, as expected and shown in Fig. S4. The displacement data again agree with eastward focusing.

To demonstrate the contribution of teleseismic waveforms in constraining the finite fault inversion, we predict these motions using a rupture model derived from the joint inversion of the geodetic and local waveform data alone (Fig. S5). We find the prediction generates poor fits to both the amplitude and timing of major teleseismic phases compared with those derived from the full inversion. For example, at stations located around an azimuth of 310° the first 15 s shows much larger amplitude than is observed. Additionally, the peak amplitude motions of the simulation arrive earlier at stations towards the north, but later towards the southeast. This test indicates that the teleseismic waveforms need to be included in the inversion to better constrain the temporal evolution of the rupture. This is particularly true for a case like Nepal where local stations are sparsely distributed in the source region.

We also test the sensitivity to the shape of source time function in the inversion by comparing the results from the cosine-shape and Kostrov-shape source time function parameterizations in Fig. 6. We
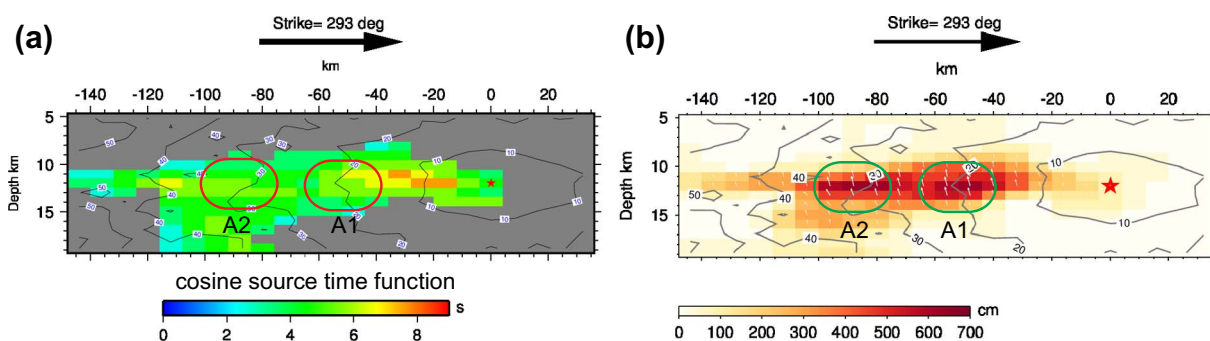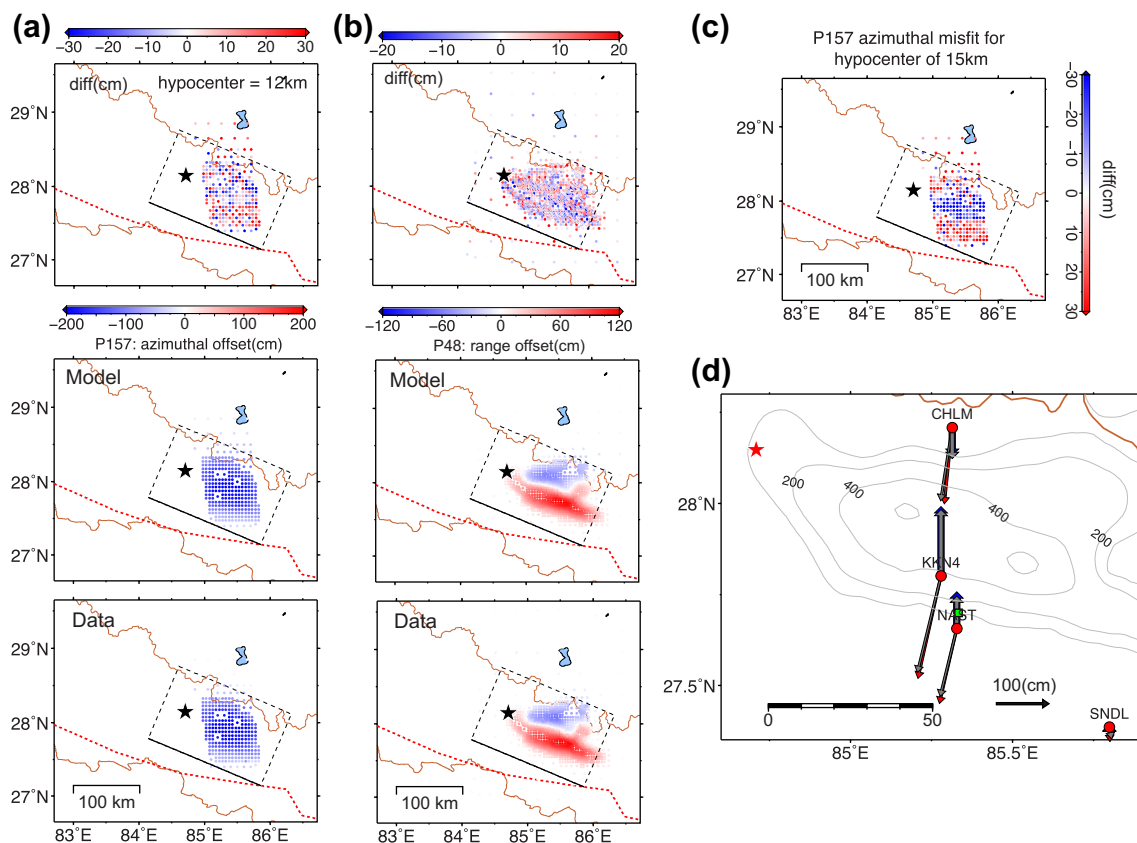

Fig. 2. (a) The smoothed rise time profiles for cosine source time function inversion. (b) Depth profile of slip distribution for inversion in (a), the contour lines indicate the rupture time. (For interpretation of the references to color in this figure legend, the reader is referred to the web version of this article.)

Fig. 3. Geodetic fits for the mainshock. Panel (a) shows the fits for azimuthal offset of ALOS-2 track P157 and (b) displays the fits and the range offset of ALOS-2 track P48. For comparison, the misfit for P157 azimuthal offsets for hypocenter depth of 15 km is given in (c) which shows distinct larger misfit. The vertical and horizontal static GPS fits are indicated in (d) with red (horizontal) and blue (vertical) indicates the synthetics and the gray indicates the observation. The slip model in Fig. 1 is shown as contours and the epicenter is displays as a red star. (For interpretation of the references to color in this figure legend, the reader is referred to the web version of this article.)

found that both source time functions produce almost identical fits for both local and teleseismic waveforms (Fig. 6b-d). This suggests that for this particular dataset with limited near source observations and for the target bandwidth of our inversion ($T > 2$ s), a cosine source time function is approximately equivalent to a Kostrov source time function with appropriate scaling since the latter function has a long tail. This may also explain the observation that inversions with a different source time function can fit the data almost equally well at relatively long period (i.e. > 5 s). However, compared with multiple-triangle source time functions inversions, our inversion scheme (single source time function) requires a much smaller number of parameters given the same subfault number. Cohee and Beroza (1994) also compared these two methods of waveform inversion and found that the single-time-function technique does a better job of recovering the true seismic moment and the average rupture velocity when tested against synthetic data.

An interesting feature in the rise time distribution is that the beginning of the fault rupture displayed larger values than the latter portion. However, such results can be affected by rupture velocity variations, as explored further in Fig. 7 assuming the Kostrov source time function. To test the potential trade-off between rise time and rupture speed, we setup the inversions at various rupture speed ranges, where the minimum rupture speed is set to 2.8 km/s (Fig. 7a), 2.5 km/s (Fig. 7b) and 2.2 km/s (Fig. 7c). However, we find that longer rise time cannot fully compensate the effect due to the increase of minimum rupture speed when the minimum speed is 2.8 km/s. For example, the horizontal component fits at station KKN4 in Fig. 7a are clearly worse than those in Fig. 7b and c. On the other hand, the difference in waveform fits becomes negligible when the minimum rupture speed decreases from 2.5 km/s to 2.2 km/s (Fig. 7b and c), while still resolving the longer rise time for the beginning portion of the rupture, although

slight tradeoffs between rise time and rupture speed can still be observed. This implies that the upper bound of the minimum rupture speed should be around 2.2–2.5 km/s, which is lower than the averaged rupture speed of the earthquake (~3.0 km/s) as also shown in the back projection results. In short, the relative slow rupture speed and/or longer rise time for the beginning of the rupture is constrained by the high quality geodetic data and the weak onset at the local strong motion data.

5. Aftershock modeling

5.1. $M_w7.2$ aftershock

The $M_w7.2$ aftershock is located to the north of the eastern end of the mainshock along with many other aftershocks, as indicated in Fig. 1. Several focal mechanisms have been reported (e.g. gCMT and USGS W-phase) for this event with similar strikes near 300° but with some variation in dip and depth. Here we used the best point source mechanism we derived from long period teleseismic P and SH wave inversion, which has a strike of 312°, a dip of 11°, and an epicentral depth of 12 km, with a Mw of 7.2. This source mechanism was used as the basis for the finite fault inversion. Here we adopted 36 P-waves and 33 SH-waves at teleseismic distance, as well as one ALOS2 descending image to conduct a joint inversion, with corresponding geodetic and waveform fits shown in Figs. 8 and 9, respectively. The overall excellent fits to both the waveform and static data indicate that the depth and slip distribution of the earthquake were well constrained.

Generally, small error of hypocenter depth is not that essential in finite fault modeling because the major slip offsets can move up or down to match the timing of depth phases (e.g. sP, sS). However, in the
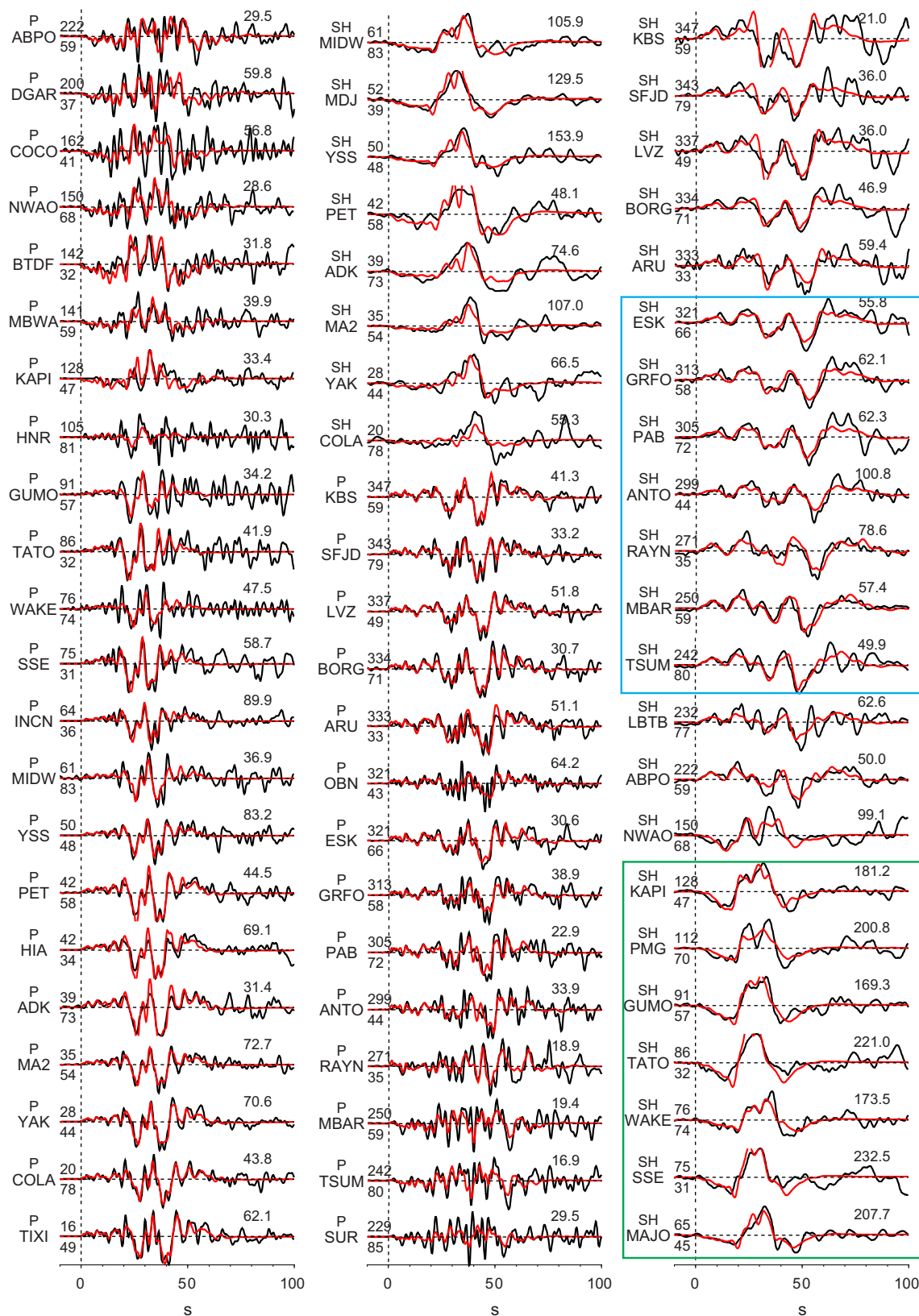
Fig. 4. Teleseismic waveform P and S-wave fits for the mainshock. The data is in black and synthetics are in red, both are in velocity and filtered to 2 s and longer period. The peak amplitude (in micrometer per second) of the data in micrometers is indicated at the end of each waveform pair. The station names are indicated at the beginning of each waveform pair along with epicenter azimuth (upper) and distance (lower).The green and blue boxes highlight the SH stations towards and away from the rupture direction, respectively. (For interpretation of the references to color in this figure legend, the reader is referred to the web version of this article.)
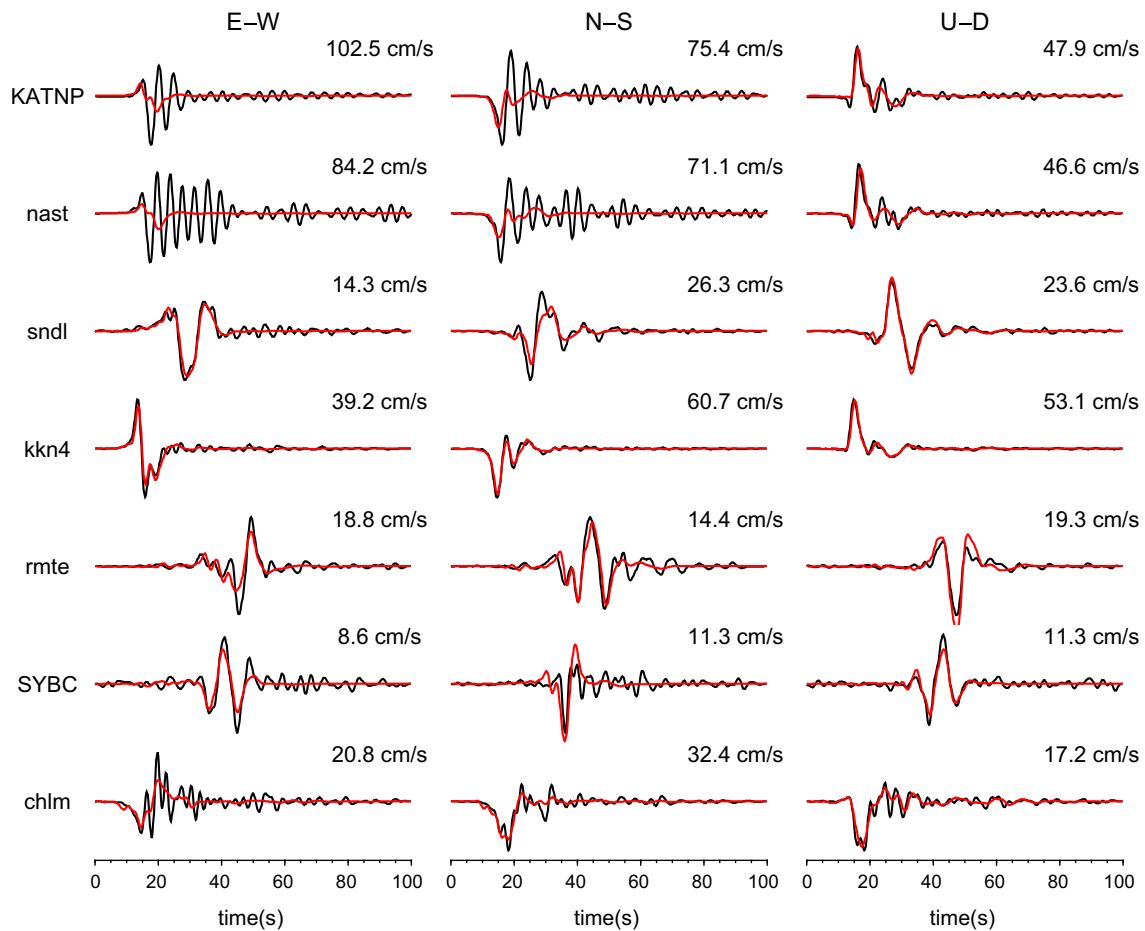
Fig. 5. Strong motion and high-rate GPS waveform fits. The data is in black and synthetic is in red, both are velocity and filtered to 3 s and longer period. The peak amplitude of the data is indicated at the end of each waveform pair. (For interpretation of the references to color in this figure legend, the reader is referred to the web version of this article.)
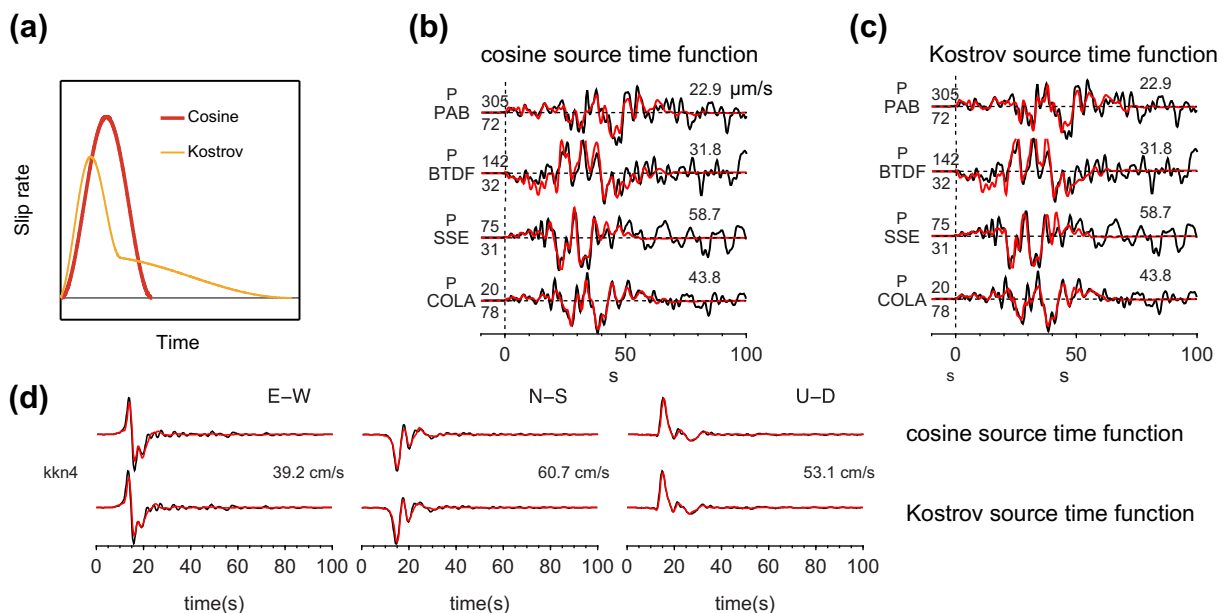

Fig. 6. (a) The shape of cosine and Kostrov source time functions, note the long tail of the latter source time function. (b) Representative teleseismic P-wave fits for cosine source time function inversion. The red is synthetic and the black is data, the amplitude of data (in micro-meter per second) is shown at the end of each waveform pair. The station and component names are indicated at the beginning of each waveform record, along with azimuth (upper) and epicenter distance (lower) in degree. (c) Similar as (a) for Kostrov source time function case. (d) High-rate GPS (differentiated to velocity) waveform fits at station KKN4 for cosine (upper) and Kostrov source time functions. Peak amplitude of each component in the data is indicated. (For interpretation of the references to color in this figure legend, the reader is referred to the web version of this article.)
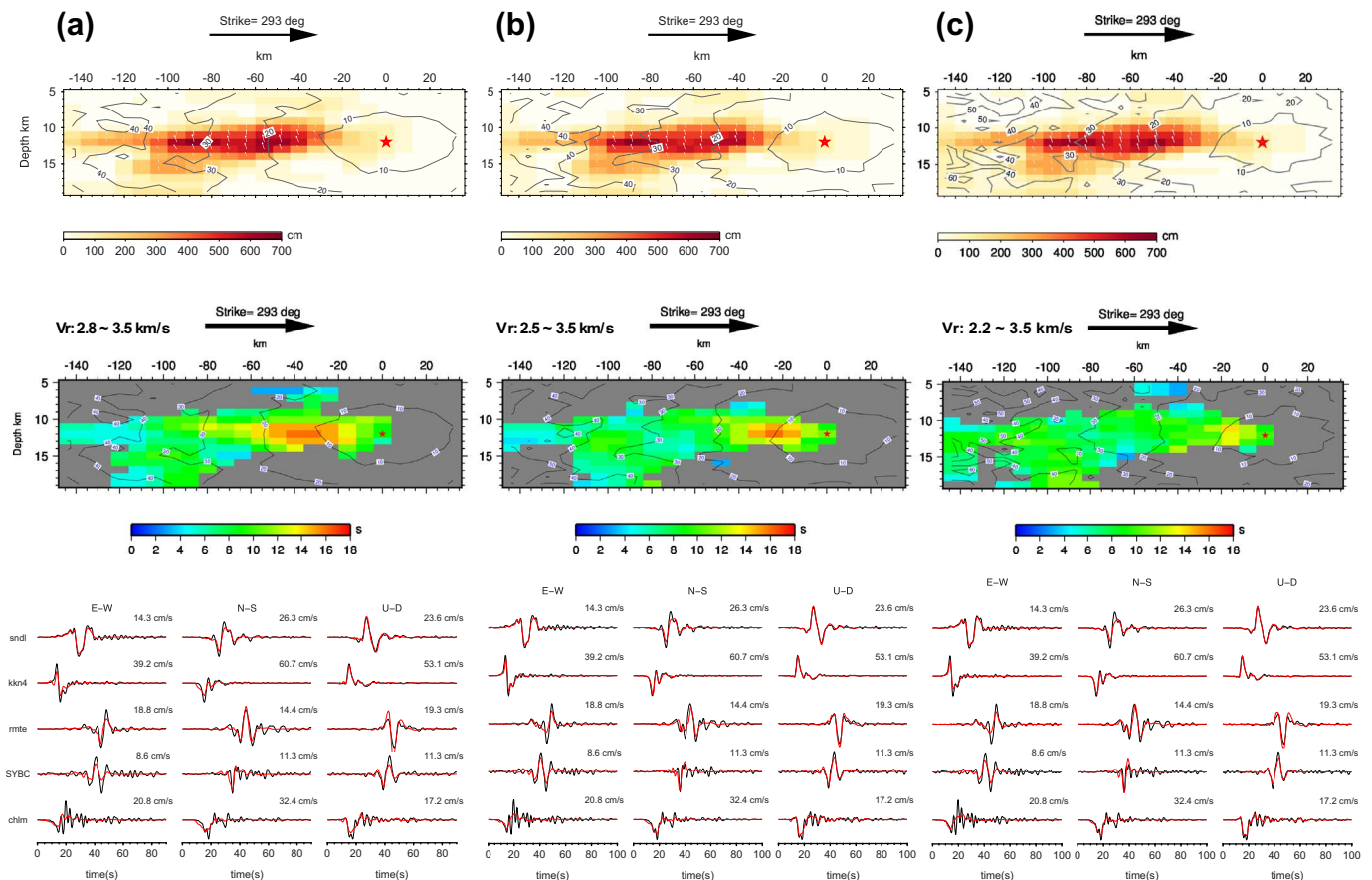
Fig. 7. Smoothed rise time distributions for the Kostrov source time function inversions, the rupture speed ranges are 2.8–3.5 km/s (a), 2.5–3.5 km/s (b) and 2.2–3.5 km/s (c). The corresponding velocity waveform fits for the local stations are shown at the bottom of each panel with data in black and synthetics in red. Peak amplitude in the data is also indicated. (For interpretation of the references to color in this figure legend, the reader is referred to the web version of this article.)

case of a low angle fault plane solution, as in this situation, the depth of hypocenter controls the interference between S and sS, etc. If we place the earthquake hypocenter at a depth of 17, the fit to the teleseismic waveforms is clearly worse than that at 12 km, in particular for the SH waves where the synthetic depth phases are later than in the data (Fig. S6). The value of 12 km can be considered as the largest depth for this earthquake since we are using a 1D velocity model without sedimentary layer, which is probably a good assumption for this region except for the Kathmandu region (Table 1). Using a slower velocity model will move the earthquake to an even shallower depth to fit the teleseismic P/SH waves and their depth phases. A depth of 12 km places the fault plane of the Mw7.2 aftershock about 5 km above the MHT, which implies that it ruptured a secondary fault shallower than the main plate boundary (Wang et al., 2017), although many other studies placed the Mw7.2 aftershock on the MHT (e.g. Baillard et al., 2017; Elliott et al., 2016).

The slip distribution of the earthquake is located to the north of the eastern end of the mainshock rupture (shown as blue contours in Fig. 1). Although the map view of their slip distributions seems complementary to each other in the north-south direction, there is a clear east-west oriented gap between them (Fig. 1). Also, note that most of the aftershocks occurred in the region surrounding the Mw7.2 aftershock, including the Mw6.7 aftershock that took place one day after the mainshock. The Mw7.2 aftershock also generated fairly strong shaking in Kathmandu, which will be discussed in the following section.

5.2. Calibration event (Mw5.2)

Although the rupture process of the Mw7.2 aftershock is relatively

simple, its source duration (Fig. 8) is still much longer than the period ranges in which we are interested (e.g. 4–5 s, the dominant frequency of basin vibration in Kathmandu). Thus, we conducted a search for a smaller event, which can be considered as a point source at the period longer than about 3 s. This proves useful in testing the performance of our Kathmandu basin model, discussed in the next section. It appears that the Mw5.2 event (latitude: 27.8297°, longitude: 85.8650°, origin time: 2015 April 26, 16:26 UTC) serves this purpose. The location of the Mw5.2 event is shown in Fig. 1.

There are several reasons we choose this specific aftershock: firstly, the horizontal location of the earthquake is well constrained as different catalogs show very similar locations (Fig. 1); secondly, the earthquake produced good signal to noise ratio in observed long period teleseismic motions, which can be used to precisely constrain the depth and focal mechanism; and thirdly, the focal mechanism of the earthquake, both from GCMT and our own inversion, shows a shallow dip angle thrust, fairly consistent with that of the mainshock. Here we used the GCMT solution and we revised the depth by modeling its teleseismic depth phases, which reveals a preferred depth of 14.5 km as demonstrated in Fig. 10. The modeling of the motions for this event within the Kathmandu basin is discussed in the next section.

6. 3D ground motion simulation for Kathmandu basin

The inversion result of the mainshock shows that the waveform fits for the basin stations KATNP and NAST, Fig. 5, are not as good as for the other local stations, as addressed in earlier studies. In particular, the horizontal components of data have much larger amplitudes and longer shaking duration (with duration defined as the time from the P-wave
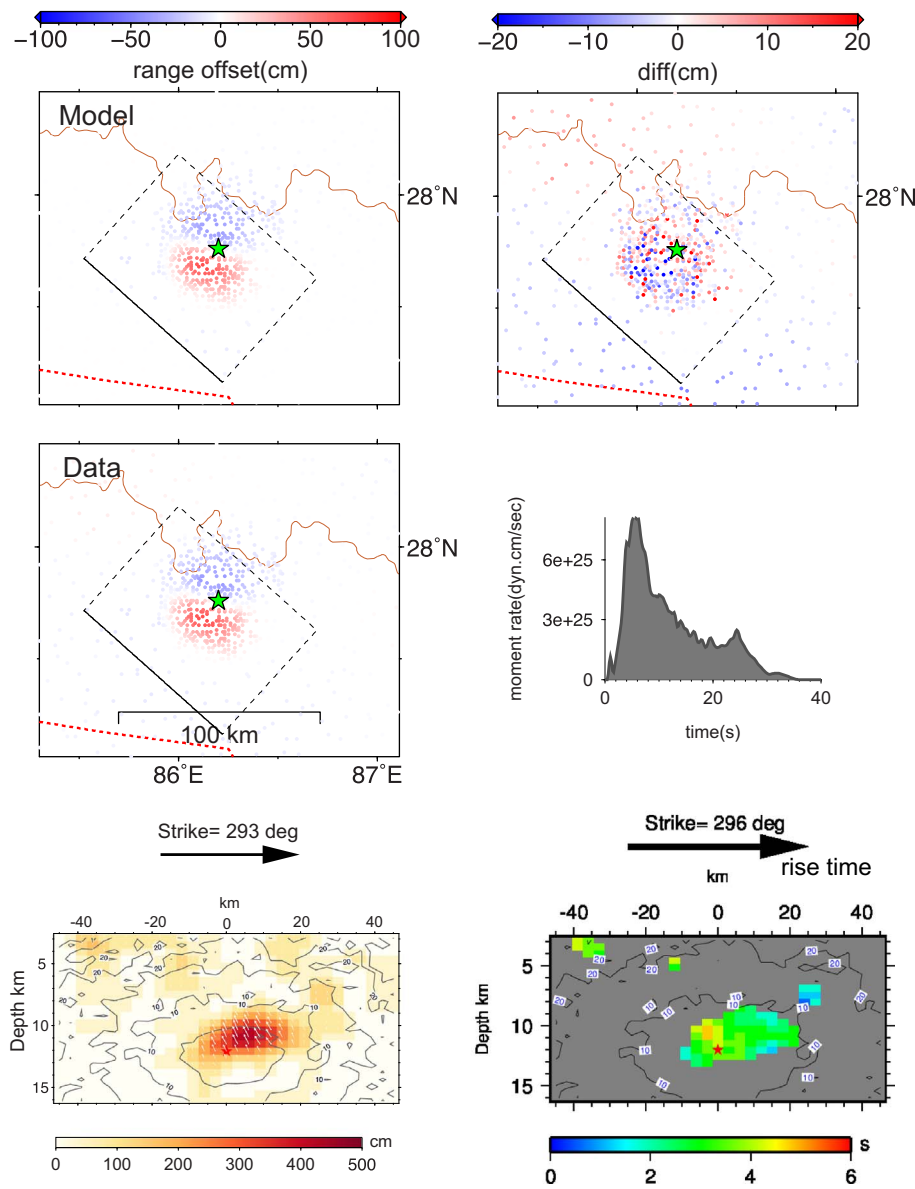
Fig. 8. InSAR fits and the moment-rate function for the Mw7.2 aftershock are shown in the upper four panels, the depth profiles of slip distribution (left) and smoothed rise time (right) are displayed at in the bottom panels.

arrival to when the coda amplitude decays to 10% of the peak ground velocity) compared with the synthetics. We suspect this is primarily caused by the sedimentary structure in the Kathmandu Valley. The waveform record for the Mw7.2 aftershock shows similar amplification features and the apparent shaking duration is even longer than that of the mainshock. The difference in the duration is possibly because the peak shaking in Kathmandu for the mainshock is dominated by the S-wave from the largest asperity that is closest to the valley while the aftershock is located further from the valley and surface waves dominate these records.

Although the basin structure appears to play an important role in the shaking, there is no available 3D velocity model in this region that includes this structure. However, Paudyal et al. (2013) have reported the thickness of soft sediment in the Kathmandu basin using micro-tremor observations, which provides key information that we use to develop a simplified 3D velocity model of the basin. To construct a 3D model in the region, we assume a 1D velocity model (Table 1) as background and use the observations from Paudyal et al. (2013) to

roughly define a simplified basin model near Kathmandu (Fig. 11). The maximum depth of the basin is about 900 m. Within the basin, we assume a layered velocity structure with 300 m of Vs = 0.4 km/s material for the top layer (See inset of Fig. 12 for our preferred model). Our modeling utilized a staggered-grid finite-difference approach Paudyal et al. (2013) with a grid spacing of 100 m.

Since the amplification of ground shaking in the basin can be sensitive to the shear wave speed, we tested different Vs values, ranging from 0.3 to 1.0 km/s with a 0.1 km/s interval, for the top layer in the basin. We found that a value of 0.4 km/s can fit the waveform of the Mw5.2 event best at 0.3 Hz and lower frequency. Although with these parameters, the maximum resolved frequency is about 0.5 Hz, we found that the observed waveforms become much more complicated above 0.3 Hz. This is clearly demonstrated in Fig. 12, where we compare the 0.3 Hz and 0.4 Hz waveforms for both synthetics and data. As seen in this figure, the shape and amplitude of synthetics change very little for different frequency bands, while it is not so for the data. This implies the simple basin model we have constructed cannot adequately capture
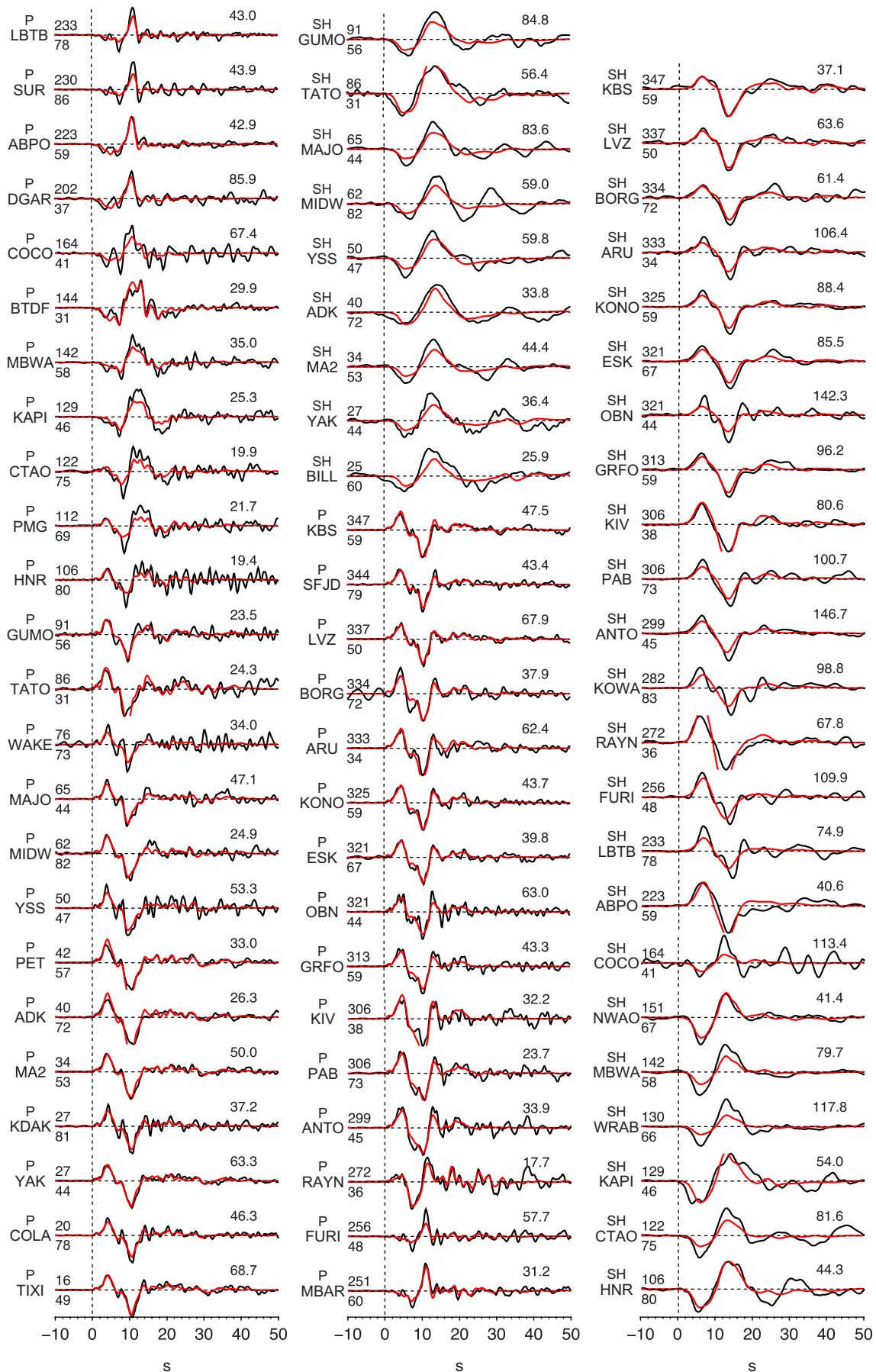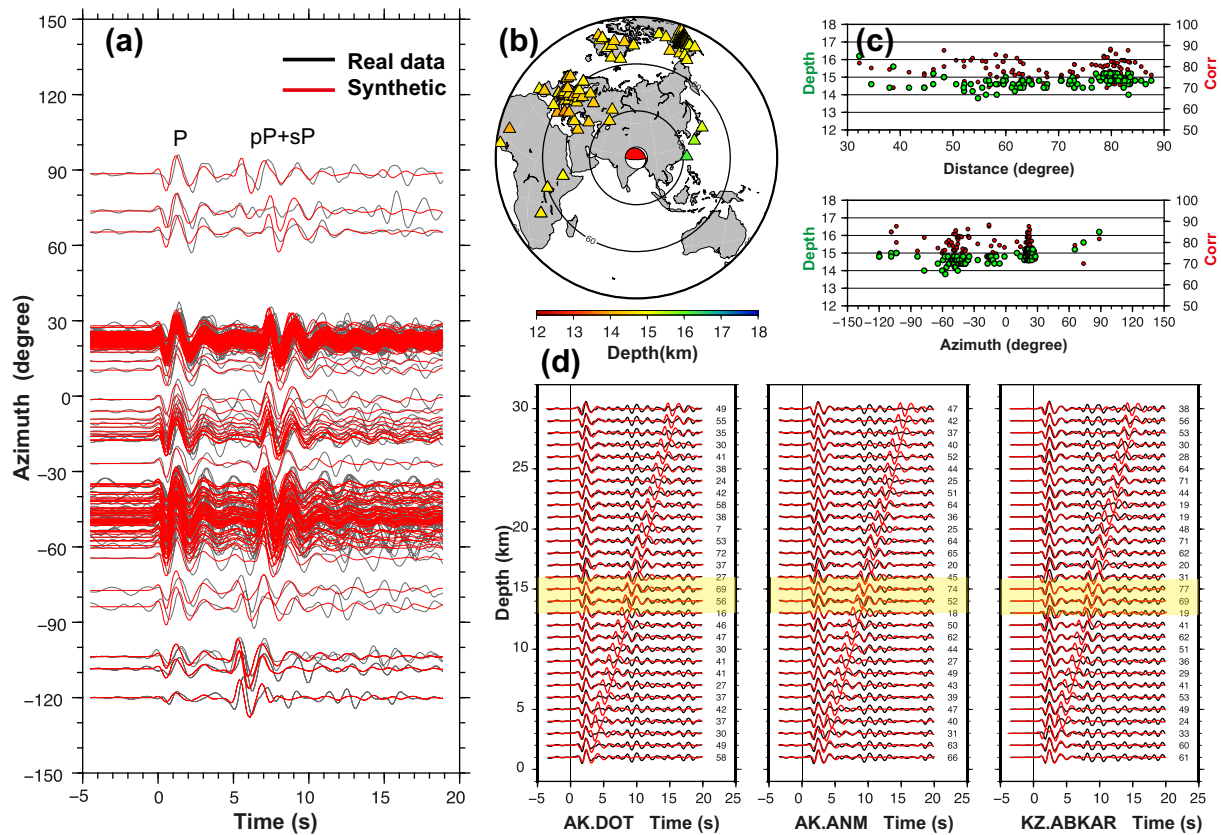
Fig. 9. Teleseismic velocity waveform fits for the Mw7.2 aftershock, see caption of Fig. 4 for more details of the descriptions. The amplitude unit is micrometer.

Fig. 10. Depth-phase modeling for the Mw5.2 aftershock, which occurred on 2015/04/26 at 16:26 (UTC). (a) The best waveform fits for teleseismic stations between the data (black) and synthetics (red), which are filtered to 0.5–1.5 Hz. (b) The telesismic station distribution. (c) The corresponding cross correlation coefficient (CC, in percentage) between the data and synthetic arranged by distance (upper) and azimuth (lower). The green and red dots represent the best depth and the corresponding CC at each station, respectively. (d) Example sensitivity tests for the depth, the CCs are shown at the end of each trace. (For interpretation of the references to color in this figure legend, the reader is referred to the web version of this article.)

the complexity in the motions at frequencies higher than 0.3 Hz, thus we will focus on 0.3 Hz and lower frequencies when we compare the synthetics with the data for the mainshock and the Mw7.2 aftershock.

Also note that, even at 0.3 Hz, the synthetics cannot reproduce the large amplitude in the data that arrived > 50 s after the P-wave, which is likely caused by the coupling of surface waves and the basin structure. A more detailed 3D velocity model is likely required to model these additional features and our current observations are too sparse to provide sufficient constraint in this regard.

With our calibrated 3D velocity model for the Kathmandu valley from the Mw5.2 event, we next perform simulations for the Mw7.2 aftershock and the mainshock using the finite-fault rupture models derived in our inversions. As guided by the calibration modeling, we restrict our comparison to frequencies of < 0.3 Hz. In this forward waveform modeling, we also included waveform records of the mainshock at additional four strong motion stations that were installed in Kathmandu by the Japanese scientists (Takai et al., 2016). The 3D synthetics and data comparisons are shown in Fig. 12, both for the mainshock and the Mw7.2 aftershock. Here we focus on the stations in the basin as the stations outside of the basin have very similar synthetics to those calculated from the 1D model discussed earlier (e.g. KKN4 in Fig. 12). As shown, the horizontal components are fit much better by the 3D synthetics both in amplitude and phase except for KTP. The horizontal 3D synthetic amplitudes at KTP are much larger than the 1D synthetics and data, as the station is located on the hard rock (Takai et al., 2016). Better waveform fits for sedimentary sites can be explained by the slower velocity structure in the basin, which bends the

incident SV and SH ray path to an almost vertical direction, thus much more S-wave energy appears on horizontal components. This is particularly true for the mainshock, as the waveform is dominated by the S waves from the asperity very close to Kathmandu. In addition, with the amplification effect due to softer material, the horizontal components in the 3D synthetics have much larger amplitudes than in the 1D synthetics. However, the vertical component shows almost the same amplitude as in the 1D synthetics and both fit the data very well.

This effect is more obvious for the mainshock, which could partly be because the amplification effect cancels out the effect due to the bending of S-waves as the projection of S-wave energy to the vertical component becomes smaller in the softer material. When a ray shoots almost vertically towards a station, the response of the structure is simpler on the vertical component than the horizontal components (e.g., receiver function effect mainly appears on horizontal components) especially when the motions are dominated by direct S arrivals as appears to be the case with the mainshock. On the other hand, we can also see that the vertical component for the Mw5.2 event shows more complexity than the mainshock and the Mw7.2 aftershock. Note that the horizontal/vertical (H/V) amplitude ratio for the Mw5.2 event is about three times larger than that for the mainshock, which is likely due to differences in radiation pattern sampling of the two events, as well as source finiteness effects.

The ground shaking animations of the mainshock and the Mw7.2 aftershock are shown in the supplement, in which the effects due to the basin structure and rupture directivity can be clearly seen. We can also see some interesting differences between the mainshock and the
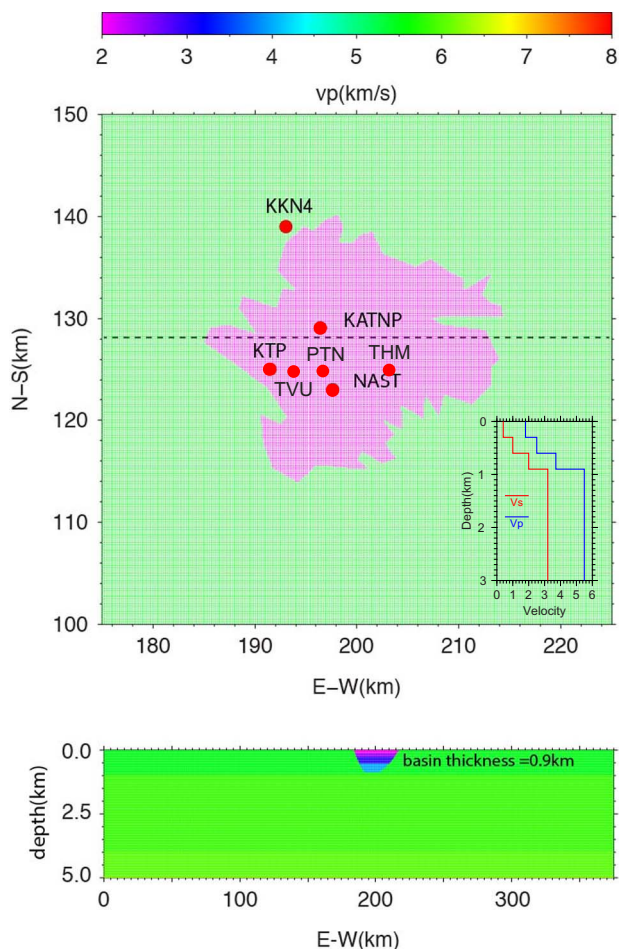
Fig. 11. 2D horizontal and vertical cuts for the P-wave velocity model used in the 3D ground motion simulation. The GPS and strong motions are indicated by the red dots. The insert shows the velocity profile in the middle of the basin. (For interpretation of the references to color in this figure legend, the reader is referred to the web version of this article.)

aftershock. The mainshock animation does not show a clear P-wave towards Kathmandu, in agreement with the very smooth onset of the observed waveform data, as well as the relatively slow and smooth beginning to the rupture process as seen in our inversions. In addition, the KATNP station is located towards the nodal direction of P-wave radiation pattern at least for the beginning portion of the rupture. Overall, the peak amplitude is dominated by the S-waves from the largest asperity that is much closer to the stations. On the other hand, the aftershock produces fairly strong P-wave amplitude towards Kathmandu and the animation clearly indicates the amplification effect in the basin.

The Peak-Ground-Velocity (PGV) maps (Fig. 13) of the two events also show very different features. As expected, the mainshock PGV shows a clear rupture directivity effect towards the ESE, while the aftershock PGV indicates slight updip rupture directivity. As shown in the animations and PGV maps, the shaking within Kathmandu Valley is much larger than that just outside of the basin, both for the mainshock and aftershock, which is due to the 3D velocity model that we used surrounding Kathmandu. The largest simulated PGV in the Kathmandu valley exceeds 100 cm/s, at relatively low frequency (< 0.5 Hz). The largest simulated PGV for the aftershock is about 40% for that of the mainshock. Due to the frequency content limit, we cannot directly

compare these simulated PGV values with the observed damage distribution since our 3D simulation does not have the high frequency content (e.g. 1–10 Hz) that most of the buildings are sensitive to. In a companion paper (Chen and Wei, 2017, summited to the same issue), the deterministic synthetics derived in this study are used to construct the broadband ground shaking synthetics, in which the relatively low frequency (> 0.5 Hz) directivity effect has been taken into account.

7. Discussion and conclusion

The dense spatial coverage and high quality of the satellite geodetic observations combined with the strong motion and teleseismic waveform records provide excellent resolution for the slip distribution and rupture process of the 2015 Nepal earthquake. Most of the published slip models, including ours, show very consistent slip distribution. The high resolution of the rupture process allows us to identify several distinct rupture stages of the mainshock, including the slow rupture propagation and long rise time occurring in the first 18 s, followed by the subsequent rupture of two large asperities located about ~40 km to the northwest and northeast of Kathmandu. We also image a deeper asperity that may overlap with the location of the 1833 rupture (Graves, 1996). The mainshock rupture appears to have had little slip at its northeastern end, where most of the aftershocks took place. These features indicate that segmentation of fault geometry may play an important role in bounding the coseismic slip, although developing a better understanding of this segmentation requires more detailed studies of the geological structure, velocity structure and seismicity. In particular, Bollinger et al. (2016) found that the coseismic slip of the mainshock matches well with the flat portion of the MHT beneath Kathmandu, and argued that the ramps on the MHT behaved as barriers during the rupture. However, whether the 1833 or 1934 events ruptured the same slip area as in 2015 event is still an open question.

Our inversion shows that we can explain the waveform data almost equally well with both cosine and Kostrov slip-rate functions. The average duration is about 6 s for the cosine source time function, which is fairly consistent with that reported by Hubbard et al. (2016). Our inversions indicate that the spatial distribution of rise time could be a robust feature since both source time function distributions (Fig. 2) show larger values (~40%) for the rupture at 5–18 s. It is interesting that some back-projection results, e.g. Galetzka et al. (2015), also show relatively slow rupture speed in this time window. As indicated by the good fits to station KKN4 and vertical component of station KATNP and NAST, the longer rise time and slow rupture speed likely leads to the weak onset and asymmetric waveform pulse recorded at these stations. The longer rise time and thus smoother rupture also suggests reduced high frequency radiation. To resolve the shape of the source time function (or slip-rate function) in greater detail we need to model the waveforms at higher frequencies, which would require a denser station coverage as well as a better understanding of the velocity structure.

Because the 2015 earthquake only ruptured the down-dip portion of the MHT, not like the case for the 1934 Mw8.4 earthquake to the east that ruptured all the way to the surface, there are still some concerns of possible future rupture on the shallow part of the MHT (Avouac et al., 2015). In addition, there is significant potential seismic hazard to the west of the 2015 earthquake, where a devastating earthquake occurred in 1505 with even longer rupture dimension than the 1934 earthquake (Avouac et al., 2015). The 1505 earthquake region has not experienced a large earthquake for > 500 years and it may be close to the end of its seismic cycle given the convergent rate of ~3 cm/year and strong coupling in the region (Bollinger et al., 2016). The slip deficit accumulated in this region is > 10 m, which if released in a single event, is larger than the peak slip of the 2015 earthquake (~7 m, see Fig. 1). Also note that 500 years is very close to the recurrence time of
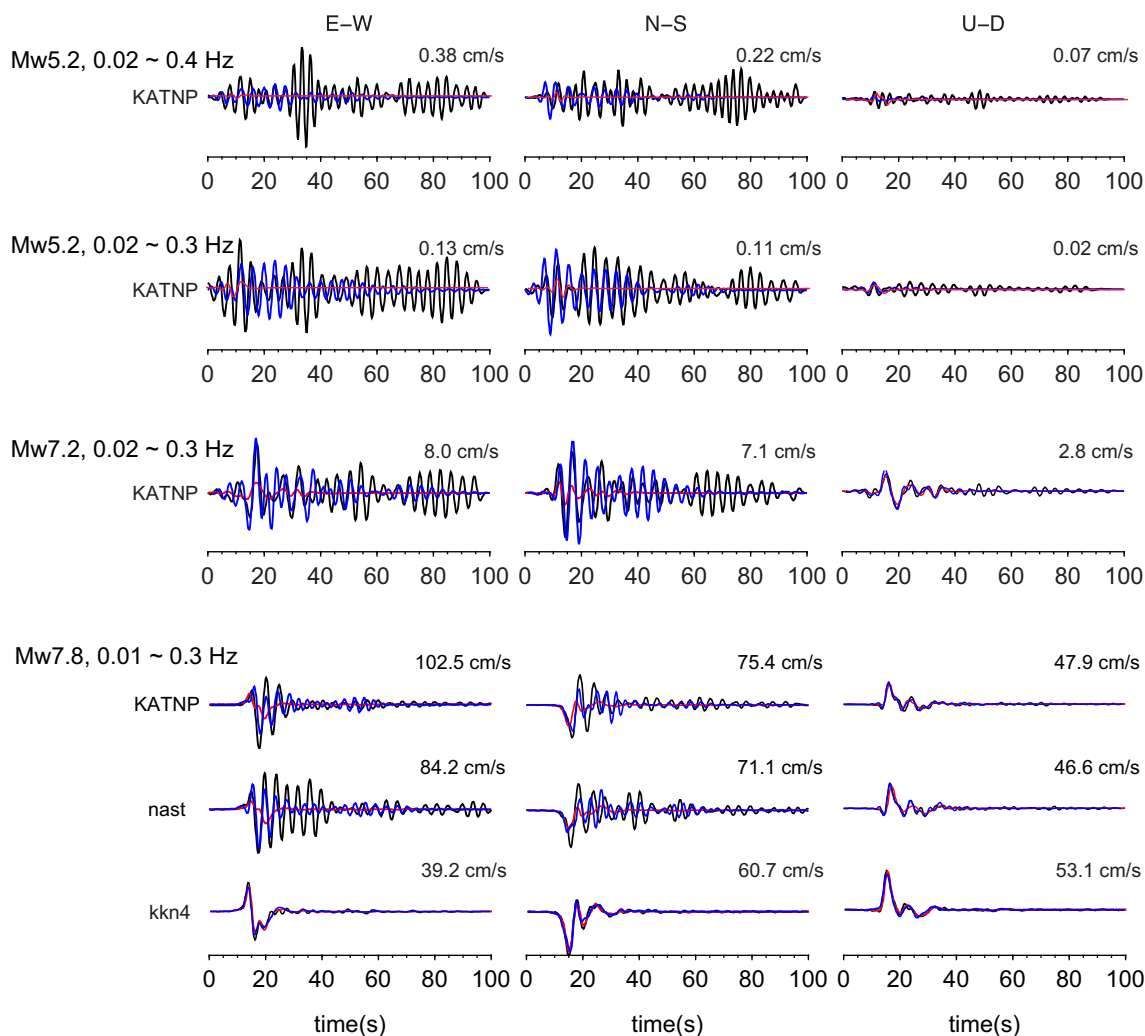
Fig. 12. Waveform fits for the Mw5.2 aftershock, the Mw7.2 event and the mainshock. All are velocity waveforms and filtered to between 0.01 Hz to 0.3 Hz except for the top panel (0.01 Hz–0.4 Hz). The 1D synthetics are shown in red and 3D synthetics are blue while the data is in black. The peak amplitude of the data is indicated at the end of each trace.

megathrust events estimated by paleoseismology and elastic modeling studies on this system, which range from 500 to 700 years (Ader et al., 2012).

The 0.2–0.25 Hz resonances of ground shaking in the Kathmandu Valley were likely a combined effect of both the source and the velocity structure. The fact that the waveform records outside of the Valley on hard rock sites show strong signals at about 0.2 Hz (e.g. station KKN4 in Fig. 5) indicates the source spectrum is dominated by energy at this frequency. The sedimentary structure within the Valley further amplifies the ground shaking, also at the dominant frequency of 0.2 Hz, suggesting the resonance frequency of the basin is around this frequency. The finite dimension of the Valley has contributed to the long duration of the ground shaking as the seismic waves were trapped in the Valley (e.g. animation 1). To model the ground shaking to higher frequency (e.g. to 10 Hz), which is more meaningful for the building damage assessments, we need to consider the strength and distribution of high frequency source radiation, as well as the effects of site response. A detailed study on the hybrid broadband ground shaking simulation of the mainshock and the Mw7.2 aftershock can be found in a companion paper (Chen and Wei, 2017), which finds that the high frequency energy was mainly radiated from the deeper portion of the rupture. This feature coupled with strong non-linear site effects led to the reduced high frequency shaking experienced in the Kathmandu Valley.

After conducting a series of finite fault inversions and ground shaking simulations for the 2015 Nepal mainshock and the Mw7.2 aftershock, we have revealed the rupture and shaking properties of these events in greater detail. Our inversions show that the coseismic slip of the mainshock has several well-constrained asperities corresponding to different stages of the rupture. In particular, the first 5–18 s of the rupture has a 40% longer rise time and slower rupture speed compared with the rest of the rupture. The 3D simulation of the strong motion and high-rate GPS stations in Kathmandu Valley indicates that a simplified 3D velocity model in Kathmandu can largely explain the vibration and amplification effect at frequencies of < 0.3 Hz, with surface layer Vs in the basin of about 400 m/s.
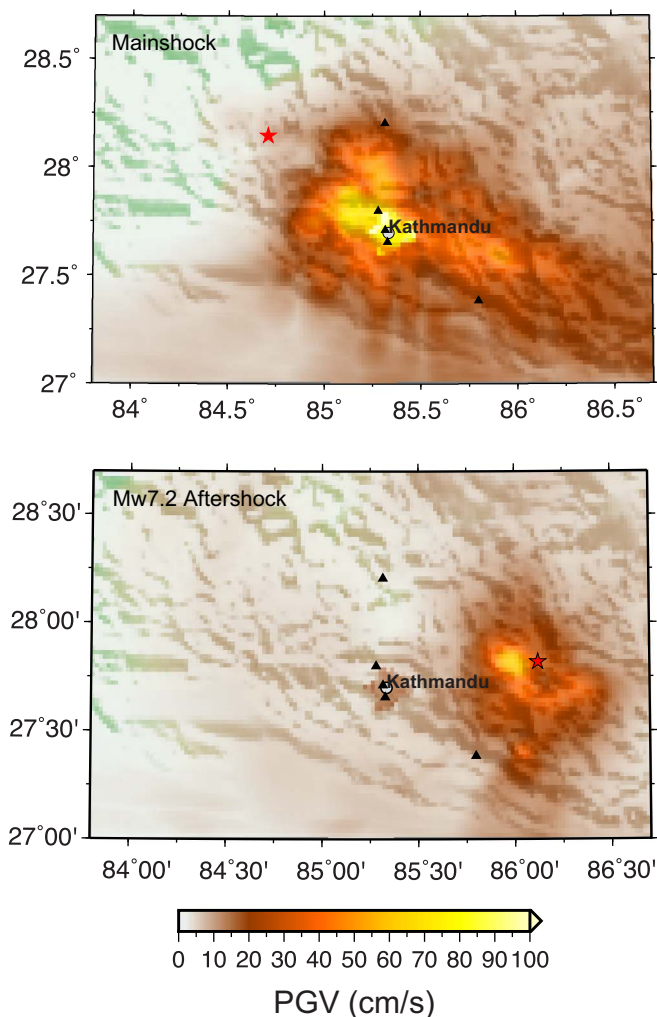
Acknowledgement

Fig. 13. Peak-Ground-Velocity maps for the mainshock and Mw7.2 aftershock, which are derived from 3D deterministic ground motion simulation (> 2 s).

Appendix A. Geodetic data processing

We processed Interferometric Synthetic Aperture Radar (InSAR) data from the Japanese Aerospace Agency (JAXA) Advanced Land Observing Satellite 2 (ALOS-2) using GMTSAR software (Chen and Wei, 2017, submitted together) and unwrapped the interferograms using SNAPHU (Sandwell et al., 2011). We used data from ascending paths 156 and 157 and descending path 48. The descending data were acquired in Wide Swath (ScanSAR) mode, enabling a swath width of 350 km, which provided complete coverage of the deformed area in a single frame. ScanSAR interferometry requires precise burst alignment between the two satellite acquisitions; ALOS-2 is the first L-band satellite to offer burst-aligned ScanSAR interferometry as a standard operating mode (Chen and Zebker, 2000). We formed interferograms from the Level 1.1 single-look-complex (SLC) images after first applying a five-parameter alignment to account for geometric and orbital errors in both range and azimuth, and ionospheric distortions which produce a second-order shift in azimuth. We found that using six or more parameters to align the image resulted in a significant phase mismatch at the sub-swath boundaries. We unwrapped each sub-swath independently using SNAPHU and then combined the sub-swaths into a single 350 km-wide image by adding an integer multiple of 2π to ensure continuous phase at the sub-swath boundaries. Some sub-swaths showed a phase discontinuity across the Himalaya Mountains related to an unwrapping error, we also resolved this by adding an integer multiple of 2π to eliminate unphysical discontinuities. The resulting interferograms from all tracks contained a residual ramp, which may be related to ionospheric distortions or orbital error; we removed a best-fitting plane from the final image after masking out the deforming area. The final interferogram products are available online at http://topex.ucsd.edu/nepal.

In addition to ALOS2 data, we also used two pairs (descending Path 19 and ascending Path 85) of Sentinel-1A Synthetic Aperture Radar (SAR) images from the European Space Agency to map the surface deformation caused by the earthquake. We aligned the post-seismic image (acquired on April 29th and May 3rd) along with the pre-seismic image (acquired on April 17th and 9th) by using the GAMMA software (Lindsey et al., 2015), and then calculated cross-correlation between uniformly distributed non-overlapping 64-by-64 sub images on the co-registered radar amplitude images. The peak location in the obtained cross correlation surface indicates the offset between the two sub-images in azimuth (satellite traveling direction) and in range (radar line-of-sight direction, LOS). Offsets between the SAR image pair are attributed to the ground displacement as well as to imaging geometry differences and topography. We therefore calculated the geometric offsets from the orbital information and the Shuttle Radar Topography Mission Digital Elevation Model (SRTM DEM).

After the geometric correction, a low-frequency trend still exists in the offsets field, probably due to inaccuracy of the orbital information. We removed this component by fitting a polynomial surface to the offsets located in the far field. We downsample the data to 263 and 715 points in azimuth and range from the descending track P19, and 499 and 786 data points from the ascending track P85, in azimuth and range, respectively. The derived range offsets measure ground displacement in the directions that are from 32 to 46° from the vertical with a component towards the west and east, while the azimuth offsets measure along-track components, which are in about SSW and NNW 11° for the descending and ascending data, respectively. The accuracy of SAR image offsets depends on the cross-correlation peak and can reach around 1/10–1/20 of the pixel spacing (Wegmuller et al., 1997). For the Sentinel-1A image, the azimuth and range pixel spacing are 14 m and 2.3 m respectively, as a consequence, azimuth offsets are only useful when the north-south component of the horizontal deformation is large, which is the case for the Nepal earthquake. Range offsets measure the surface deformation in the same direction as interferogrammetry, which can be formed from the same SAR image pair. However the C-band phase information is seriously decorrelated in the Himalayan mountainous areas. In addition, the high deformation gradient surrounding the peak deforming area may result in aliasing phase values. Both factors can cause un-reliable phase unwrapping results, we therefore decide to use image offset data for our model inversion.

Appendix B. Supplementary data

Supplementary data to this article can be found online at https://doi.org/10.1016/j.tecto.2017.11.024.

References

Ader, T., Avouac, J.P., Liu-Zeng, J., Lyon-Caen, H., Bollinger, L., Galetzka, J., Genrich, J., Thomas, M., Chanard, K., Sapkota, S.N., Rajaure, S., Shrestha, P., Ding, L., Flouzat, M., 2012. Convergence rate across the Nepal Himalaya and interseismic coupling on the Main Himalayan Thrust: implications for seismic hazard. J. Geophys. Res. Solid Earth 117.

Avouac, J.P., Meng, L.S., Wei, S.J., Wang, T., Ampuero, J.P., 2015. Lower edge of locked Main Himalayan Thrust unzipped by the 2015 Gorkha earthquake. Nat. Geosci. 8, 708–711.

Baillard, C., Lyon-Caen, H., Bollinger, L., Rietbrock, A., Letort, J., Adhikari, L.B., 2017. Automatic analysis of the Gorkha earthquake aftershock sequence: evidences of structurally segmented seismicity. Geophys. J. Int. 209, 1111–1125.

Bettinelli, P., Avouac, J.P., Flouzat, M., Jouanne, F., Bollinger, L., Willis, P., Chitrakar, G.R., 2006. Plate motion of India and interseismic strain in the Nepal Himalaya from GPS and DORIS measurements. J. Geod. 80, 567–589.

Bollinger, L., Avouac, J.P., Beyssac, O., Catlos, E.J., Harrison, T.M., Grove, M., Goffe, B., Sapkota, S., 2004. Thermal structure and exhumation history of the Lesser Himalaya

in central Nepal. Tectonics 23.

Bollinger, L., Tapponnier, P., Sapkota, S.N., Klinger, Y., 2016. Slip deficit in central Nepal: omen for a repeat of the 1344 AD earthquake? Earth Planets Space 68.

Cattin, R., Avouac, J.P., 2000. Modeling mountain building and the seismic cycle in the Himalaya of Nepal. J. Geophys. Res. Solid Earth 105, 13389–13407.

Chen, M., Wei, S.J., 2017. Broadband Simulation of the 2015 Gorkha (Nepal) Earthquake Sequence: II. Hybrid Approach for Ground Shaking Tectonophysics.

Chen, C.W., Zebker, H.A., 2000. Network approaches to two-dimensional phase unwrapping: intractability and two new algorithms. J. Opt. Soc. Am. A Opt. Image Sci. Vis. 17, 401–414.

Cohee, B., Beroza, G.C., 1994. A comparison of two methods for earthquake source inversion using strong motion seismograms. Ann. Geophys. 37, 1515–1538.

Elliott, J.R., Jolivet, R., Gonzalez, P.J., Avouac, J.P., Hollingsworth, J., Searle, M.P., Stevens, V.L., 2016. Himalayan megathrust geometry and relation to topography revealed by the Gorkha earthquake. Nat. Geosci. 9, 174–180.

Fan, W.Y., Shearer, P.M., 2015. Detailed rupture imaging of the 25 April 2015 Nepal earthquake using teleseismic P waves. Geophys. Res. Lett. 42, 5744–5752.

Feng, G.C., Li, Z.W., Shan, X.J., Zhang, L., Zhang, G.H., Zhu, J.J., 2015. Geodetic model of the 2015 April 25 M-w 7.8 Gorkha Nepal Earthquake and M-w 7.3 aftershock estimated from InSAR and GPS data. Geophys. J. Int. 203, 896–900.

Galetzka, J., Melgar, D., Genrich, J.F., Geng, J., Owen, S., Lindsey, E.O., Xu, X., Bock, Y., Avouac, J.P., Adhikari, L.B., Upreti, B.N., Pratt-Sitaula, B., Bhattarai, T.N., Sitaula, B.P., Moore, A., Hudnut, K.W., Szeliga, W., Normandeau, J., Fend, M., Flouzat, M., Bollinger, L., Shrestha, P., Koirala, B., Gautam, U., Bhatterai, M., Gupta, R., Kandel, T., Timsina, C., Sapkota, S.N., Rajaure, S., Maharjan, N., 2015. Slip pulse and resonance of the Kathmandu basin during the 2015 Gorkha earthquake, Nepal. Science 349, 1091–1095.

Grandin, R., Vallee, M., Satriano, C., Lacassin, R., Klinger, Y., Simoes, M., Bollinger, L., 2015. Rupture process of the M-w = 7.9 2015 Gorkha earthquake (Nepal): insights into Himalayan megathrust segmentation. Geophys. Res. Lett. 42, 8373–8382.

Graves, R.W., 1996. Simulating seismic wave propagation in 3D elastic media using staggered grid finite differences. Bull. Seismol. Soc. Am. 86, 1091–1106.

Hayes, G.P., Briggs, R.W., Barnhart, W.D., Yeck, W.L., McNamara, D.E., Wald, D.J., Nealy, J.L., Benz, H.M., Gold, R.D., Jaiswal, K.S., Marano, K., Earle, P.S., Hearne, M.G., Smoczyk, G.M., Wald, L.A., Samsonov, S.V., 2015. Rapid characterization of the 2015 M-w 7.8 Gorkha, Nepal, earthquake sequence and its seismotectonic context. Seismol. Res. Lett. 86, 1557–1567.

Hubbard, J., Almeida, R., Foster, A., Sapkota, S.N., Burgi, P., Tapponnier, P., 2016. Structural segmentation controlled the 2015 M-w 7.8 Gorkha earthquake rupture in Nepal. Geology 44, 639–642.

Ji, C., Wald, D.J., Helmberger, D.V., 2002. Source description of the 1999 Hector Mine, California, earthquake, part I: wavelet domain inversion theory and resolution analysis. Bull. Seismol. Soc. Am. 92, 1192–1207.

Lave, J., Avouac, J.P., 2000. Active folding of fluvial terraces across the Siwaliks Hills, Himalayas of central Nepal. J. Geophys. Res. Solid Earth 105, 5735–5770.

Lay, T., Ye, L.L., Koper, K.D., Kanamori, H., 2017. Assessment of teleseismically-determined source parameters for the April 25, 2015 MW 7.9 Gorkha, Nepal earthquake and the May 12, 2015 MW 7.2 aftershock. Tectonophysics 714, 4–20.

Lindsey, E.O., Natsuaki, R., Xu, X.H., Shimada, M., Hashimoto, M., Melgar, D., Sandwell, D.T., 2015. Line-of-sight displacement from ALOS-2 interferometry: M-w 7.8 Gorkha Earthquake and M-w 7.3 aftershock. Geophys. Res. Lett. 42, 6655–6661.

Liu, C.L., Zheng, Y., Wang, R.J., Shan, B., Xie, Z.J., Xiong, X., Ge, C., 2016. Rupture processes of the 2015 Mw 7.9 Gorkha earthquake and its Mw 7.3 aftershock and their implications on the seismic risk. Tectonophysics 382, 264–277.

Mahesh, P., Rai, S.S., Sivaram, K., Paul, A., Gupta, S., Sarma, R., Gaur, V.K., 2013. One-dimensional reference velocity model and precise locations of earthquake hypocenters in the Kumaon-Garhwal Himalaya. Bull. Seismol. Soc. Am. 103, 328–339.

Martin, S.S., Hough, S.E., Hung, C., 2015. Ground motions from the 2015 M-w 7.8 Gorkha, Nepal, earthquake constrained by a detailed assessment of macroseismic data. Seismol. Res. Lett. 86, 1524–1532.

McGowan, S.M., Jaiswal, K.S., Wald, D.J., 2017. Using structural damage statistics to derive macroseismic intensity within the Kathmandu valley for the 2015 M7. 8 Gorkha, Nepal earthquake. Tectonophysics 714, 158–172.

Paudyal, Y.R., Yatabe, R., Bhandary, N.P., Dahal, R.K., 2013. Basement topography of the Kathmandu Basin using microtremor observation. J. Asian Earth Sci. 62, 627–637.

Sandwell, D., Mellors, R., Tong, X., Wei, M., Wessel, P., 2011. Gmtsar: an insar processing system based on generic mapping tools. In: Scripps Institution of Oceanography Technical Report.

Sapkota, S.N., Bollinger, L., Klinger, Y., Tapponnier, P., Gaudemer, Y., Tiwari, D., 2013. Primary surface ruptures of the great Himalayan earthquakes in 1934 and 1255 (vol 6, pg 71, 2013). Nat. Geosci. 6, 152.

Sapkota, S.N., Bollinger, L., Perrier, F., 2016. Fatality rates of the M-w similar to 8.2, 1934, Bihar-Nepal earthquake and comparison with the April 2015 Gorkha earthquake. Earth Planets Space 68.

Takai, N., Shigefuji, M., Rajaure, S., Bijukchhen, S., Ichiyanagi, M., Dhital, M.R., Sasatani, T., 2016. Strong ground motion in the Kathmandu Valley during the 2015 Gorkha, Nepal, earthquake. Earth Planets Space 68.

Wang, K., Fialko, Y., 2015. Slip model of the 2015 M-w 7.8 Gorkha (Nepal) earthquake from inversions of ALOS-2 and GPS data. Geophys. Res. Lett. 42, 7452–7458.

Wang, X., Wei, S.J., Wu, W.B., 2017. Double-ramp on the Main Himalayan Thrust revealed by broadband waveform modeling of the 2015 Gorkha earthquake sequence. Earth Planet. Sci. Lett. 473, 83–93.

Wegmuller, U., Werner, C.L., Esa, 1997. Third Ers Symposium on Space at the Service of Our. Vols. Ii & Iii Vol. 414 Esa Special Publications.

Wei, S.J., Helmberger, D., Zhan, Z.W., Graves, R., 2013. Rupture complexity of the M-w 8.3 Sea of Okhotsk earthquake: rapid triggering of complementary earthquakes? Geophys. Res. Lett. 40, 5034–5039.

Yagi, Y., Okuwaki, R., 2015. Integrated seismic source model of the 2015 Gorkha, Nepal, earthquake. Geophys. Res. Lett. 42, 6229–6235.

Yue, H., Simons, M., Duputel, Z., Jiang, J.L., Fielding, E., Liang, C., Owen, S., et al., 2017. Depth varying rupture properties during the 2015 Mw 7.8 Gorkha (Nepal) earthquake. Tectonophysics 714, 44–54.